Proceedings of the ASME 2020 International Design Engineering Technical Conferences & Computers and Information in Engineering Conference
IDETC/CIE 2020
August 16-19, 2020, St. Louis, USA

IDETC2020-16019

DEFORMABLE BLADE ELEMENT AND UNSTEADY VORTEX LATTICE FLUID-STRUCTURE INTERACTION MODELING OF A 2D FLAPPING WING

Joseph Reade
Graduate Researcher
josephreade.school@gmail.com

Mark A. Jankauski
Assistant Professor
mark.jankauski@montana.edu

ABSTRACT

Flapping insect wings experience appreciable deformation due to aerodynamic and inertial forces. This deformation is believed to benefit the insect's aerodynamic force production as well as energetic efficiency. However, the fluid-structure interaction (FSI) models used to estimate wing deformations are often computationally demanding and are therefore challenged by parametric studies. Here, we develop a simple FSI model of a flapping wing idealized as a two-dimensional pitching-plunging airfoil. Using the Lagrangian formulation, we derive the reduced-order structural framework governing wing's elastic deformation. We consider two fluid models: quasi-steady Deformable Blade Element Theory (DBET) and Unsteady Vortex Lattice Method (UVLM). DBET is computationally economical but does not provide insight into the flow structure surrounding the wing, whereas UVLM approximates flows but requires more time to solve. For simple flapping kinematics, DBET and UVLM produce similar estimates of the aerodynamic force normal to the surface of a rigid wing. More importantly, when the wing is permitted to deform, DBET and UVLM agree well in predicting wingtip deflection and aerodynamic normal force. The most notable difference between the model predictions is a roughly 20° phase difference in normal force. DBET estimates wing deformation and force production approximately 15 times faster than UVLM for the parameters considered, and both models solve in under a minute when considering 15 flapping periods. Moving forward, we will benchmark both low-order models with respect to high fidelity computational fluid dynamics coupled to finite element analysis, and assess the agreement between DBET and UVLM over a broader range of flapping kinematics.

INTRODUCTION

Over the past decade, flying insects have become a popular model organism for bio-inspired flapping wing micro air vehicles (FWMAVs) [1]. Unlike rotor based aircraft, which suffer inefficiencies that preclude their flight at reduced length scales and low Reynolds numbers, FWMAVs can scale down almost indefinitely due to the unsteady aerodynamic mechanisms enabled by their flapping wings [2]. This makes FWMAVs a desirable platform for tasks that require the vehicle to operate in congested environments, for example infrastructure monitoring of piping networks. Nonetheless, while researchers have developed successful insect-scale FWMAVs, there remain several design challenges that must be overcome before such vehicles are suitable for widespread applications. Some of these challenges include reducing energetic expenditures, implementing reliable on-board control systems and improving aircraft durability. A better understanding of insect flight, in particular the flapping wing, can guide engineering design to surmount many of these challenges.

As an insect wing flaps, it deforms from both aerodynamic and inertial forces [3]. Wing deformation has been shown to provide numerous advantages to flight, including improving aerodynamic force production [4] and reducing energetic costs [5]. In some insects, wing deformation provides a sensing modality as well. Hawkmoth *Manduca sexta* wings are imbued with mechanoreceptors called campaniform sensilla, and recent studies show the feedback encoded by these receptors facilitate the insect's attitude control system [6]. The insect wing may therefore behave both as a sensor and an actuator in some contexts. Despite the significance of wing flexibility to flapping wing flight, however, the mathematical models used to predict flapping wing fluid-structure interaction (FSI) remain limited.

The most common flapping FSI models utilize finite element analysis (FEA) coupled to computational fluid dynamics (CFD) to estimate wing deformation and to resolve the flow field surrounding the flexible structure [7–9]. While such models are instrumental to improving the knowledge of flexible wing dynamics, they are often computationally inefficient, sometimes taking hours or days to solve. With respect to FEA, the periodic rotations of the wing give rise to centrifugal softening, which cause the structural stiffness matrix to become time-varying [10, 11]. As a result, the stiffness matrix must be updated at each interval of analysis, which in turn increases the time required to solve for wing deformation. With respect to CFD, upwards of tens of thousands of equations must be solved to resolve the entire flow field surrounding a flapping wing [12]. Moreover, the CFD mesh must generally be restructured as the wing passes through it. Clearly, both fluid and structural solvers require considerable computational resources, and these computational requirements become nearly intractable when fluid and structure are coupled.

To reduce these computational requirements, the flapping wing is often simplified to a two-dimensional problem. A flapping wing in two dimensions emulates a pitching, plunging airfoil, where the length of the airfoil is the mean chord width of the insect wing. While some of the physics associated with flapping in three-dimensions are lost, the two-dimensional pitch-plunge model has been used to garner many insights into flapping wing flight. Yin and Luo utilized a 2D FSI model to study the effect of wing inertial forces on deformation and the resulting aerodynamic forces during hover [13]. Tian et al. extended this work to address the influence of wing flexibility during forward flight [14]. Sridhar and Kang used a 2D FSI model to investigate energy expenditures in flapping fruit flies [15]. Despite the two-dimensional idealization, however, these FSI models are still computationally expensive because of their reliance on CFD and FEA. Studies investigating broad ranges of wing kinematics, flexibility or other parameters may be challenged by these high-order methods depending on the desired number of variables considered.

To enable parametric studies of flapping wings, many researchers have turned to more efficient structural and fluid modeling. While modal reduction is almost exclusively used to reduce the demands of the structural solver [10, 11, 16], the fluid models employed to supplement CFD are more varied. The two most common tend to be based upon blade element theory (BET) and unsteady vortex lattice method (UVLM). BET functions by discretizing a wing into chord-wise airfoils, or "blade elements". Differential forces are estimated via airfoil theory for each blade element and are summed over the entire to wing to estimate total aerodynamic forces. While BET is among the most widely used models for flapping wing flight, it is typically restricted to rigid wings with only a handful of exceptions. Wang et al. developed an economical flapping wing FSI model using a blade element aerodynamic approach, however their model permits only wing twisting and not bending [17]. Schwab et al. developed and experimentally validated a BET-based FSI model, however it was applicable only to single-degree-of-freedom flapping that did not generate lift [18, 19]. This model was later extended to 3D kinematics, but considered only unilateral coupling between fluid and structure [20]. Thus, it remains to be seen if BET can concurrently model bilateral fluid-structure coupling as well as lift-generating 2D flapping.

The other common reduced-order fluid model is UVLM. UVLM is a numerical method that discretizes the wing into panels, each to which a vortex is bound. By estimating the strength of each bound and shed vortex, one can estimate the pressure distribution over a wing. Fitzgerald et al. derived a UVLM-based 2D flapping FSI model, and found that UVLM made flow predictions similar to those made by direct numerical simulation for the deforming wing [21]. They utilized a structural model composed of two rigid links connected by a torsional spring. Mountcastle and Daniel utilized a similar 2D UVLM FSI model with additional links to determine the effect of structural flexibility on flapping wing lift generation [22]. They found that the additional force generation attributed to wing flexibility was sensitive to the relative phase of pitch and plunge. Despite the success of UVLM in flapping wing FSI models, it still requires more computational time relative to BET. It is presently unknown if BET and UVLM produce similar results when modeling flexible wings.

Based upon this literature review, there remains a need for a 2D pitch-plunge flapping wing FSI model that (1) is reduced order to facilitate broad parametric studies and (2) able to accommodate arbitrary planar geometries with spatially varying properties. The objective of the present work is to develop this model. We put forward two candidate approaches – the first based on BET, which we refer to as deformable blade element theory (DBET) owing to its capacity to account for deformation, and the second based on UVLM, which is typically considered a higher-fidelity fluid solver relative to BET. This manuscript presents the first effort towards a tiered "family of models" for flexible pitching-plunging airfoils. Moving forward, we intend to benchmark both of these reduced-order FSI models with respect to high-fidelity, high computational demand CFD. This "family of models" approach will illustrate the trade-offs between solution accuracy and economy within the context of 2D flapping wing FSI.

The remainder of the paper is organized as follows. First, we derive the equation of motion governing the wing dynamics via the Lagrangian formulation. We then outline the DBET and UVLM fluid models used to estimate aerodynamic forces acting on the flexible wing. Next, compare the two models and how they predict wing deformation and aerodynamic force production. We conclude by discussing the implications and future directions of our modeling efforts.

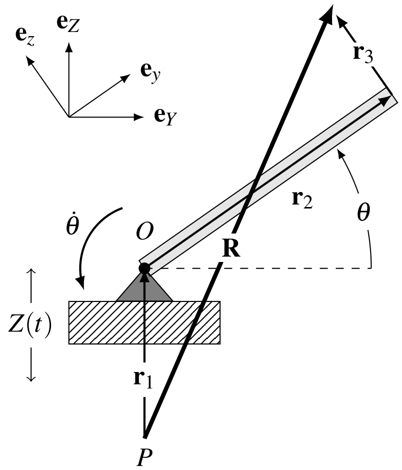

FIGURE 1. Diagram of flexible wing undergoing prescribed rigid body pitching (θ) and plunging (Z).

THEORY

Here, we derive a mathematical model to predict the elastic deformation of a pitching, plunging flexible wing. We first define the rigid body kinematics of the wing, and determine the equation of motion governing the deflection of the wing via the Lagrangian formulation. We then describe the DBET and UVLM fluid models used to estimate fluid loading on the wing surface and to calculate aerodynamic forces.

Structural Model

First, we establish a rotating, translating coordinate frame that moves with the rigid body motion of the wing (Fig. 1). Consider a fixed point P and a translating point O about which the wing is free to rotate. We define O as the origin of the wing-bound reference frame. The displacement of O is described by the prescribed plunging motion of the wing $Z(t)$. Then, the reference frame bound to O is subjected to a positive counter-clockwise rotation by a pitching angle $\theta(t)$. The resulting $x-y-z$ reference frame has an angular velocity $\mathbf{\Omega}$ defined by

$$\mathbf{\Omega} = \dot{\theta}\mathbf{e}_x \tag{1}$$

Within the $x-y-z$ frame, we draw a position vector $\mathbf{R}$ from fixed point P to a differential mass element dm located on the flexible wing. $\mathbf{R}$ is the sum of three intermediate position vectors such that $\mathbf{R} = \mathbf{r}_1 + \mathbf{r}_2 + \mathbf{r}_3$, where

$$\mathbf{r}_1 = Z(t)\,\mathbf{e}_Z = Z(t)[\sin\theta\,\mathbf{e}_y + \cos\theta\,\mathbf{e}_z] \tag{2}$$

$$\mathbf{r}_2 = y\,\mathbf{e}_y; \quad 0 \le y \le c \tag{3}$$

$$\mathbf{r}_3 = W(y,t)\,\mathbf{e}_z \tag{4}$$

Above, $\mathbf{r}_1$ denotes to the prescribed vertical plunging of the rotational pivot point O, $\mathbf{r}_2$ denotes the y position of dm along the flexible wing between zero and max chord-width c, and $\mathbf{r}_3$ denotes an infinitesimal out-of-plane elastic deflection dependent on both space and time. The velocity of the differential mass with respect to the rotating coordinate frame is

$$\dot{\mathbf{R}} = \mathbf{\Omega} \times \mathbf{R} + \dot{\mathbf{r}}_1 + \dot{\mathbf{r}}_3 \tag{5}$$

$$\dot{\mathbf{R}} = [\dot{Z}\sin\theta - W\dot{\theta}]\,\mathbf{e}_y + [\dot{Z}\cos\theta + y\dot{\theta} + \dot{W}]\,\mathbf{e}_z \tag{6}$$

We also determine the acceleration of the differential mass as

$$\begin{aligned}\ddot{\mathbf{R}} &= (\ddot{Z}\sin\theta - 2\dot{W}\dot{\theta} - W\ddot{\theta} - y\dot{\theta}^2)\mathbf{e}_y \\ &\cdots + (\ddot{Z}\cos\theta + y\ddot{\theta} - W\dot{\theta}^2 + \ddot{W})\mathbf{e}_z\end{aligned} \tag{7}$$

Note that $\ddot{\mathbf{R}}$ is not required to formulate the equation of motion governing wing deformation, however it needed later to approximate the added mass fluid loading. Next, we discretize out-of-plane deflection W via an eigenfunction expansion of vibration mode shapes $\phi_k(y)$ multiplied by modal responses $q_k(t)$, or

$$W(y,t) = \sum_{k=1}^{\infty} \phi_k(y) q_k(t) \tag{8}$$

where vibration mode shapes are normalized with respect to the wing's mass to satisfy orthonormal conditions. We then formulate wing's potential and kinetic energies, which are required to employ the Lagrangian approach. Note that only a high-level derivation is provided here; for further detail on the equation of motion derivation, please refer to Appendix A. The kinetic energy T of the flexible wing is

$$T = \frac{1}{2}\int_m \dot{\mathbf{R}} \cdot \dot{\mathbf{R}}\,dm \tag{9}$$

where Eqs. 6 and 8 are substituted into the above expression to give the explicit form of T. The potential energy U of the wing is

$$U = \frac{1}{2}\int_V S(W,W)\,dV \tag{10}$$

where V is the volumetric domain of integration, and S is a symmetric, quadratic strain energy density function. Using the Lagrangian approach, we determine the Equation of Motion (EoM) governing the unknown modal response q_k as

$$\ddot{q}_k + (\omega_k^2 - \dot{\theta}^2)q_k = -\lambda_k \ddot{Z}\cos\theta - \psi_k \ddot{\theta} + Q_k \tag{11}$$

where Q_k is the non-conservative aerodynamic force projected onto the wing's kth mode, ω_k is the wing's kth natural frequency and λ_k, ψ_k are constants defined by

$$\lambda_k = \int_m \phi_k \, dm \tag{12}$$

$$\psi_k = \int_m y\, \phi_k \, dm \tag{13}$$

The non-conservative aerodynamic modal force is determined through the principle of virtual work, where the virtual work $\delta\mathcal{W}$ is

$$\delta\mathcal{W} = Q_k \delta q_k \tag{14}$$

$$Q_k \delta q_k = \int_S \mathbf{F}_N \cdot \delta W \mathbf{e}_z \, dS = \int_S \mathbf{F}_N \cdot \sum_{k=1}^{\infty} \phi_k \delta q_k \, \mathbf{e}_z \, dS \tag{15}$$

$$Q_k = \int_S \phi_k \mathbf{F}_N \cdot \mathbf{e}_z \, dS \tag{16}$$

where $\mathbf{F}_N$ is the physical aerodynamic force, S is the surface over which the aerodynamic force acts, and all quantities preceded by a δ are virtual quantities. Note that $\mathbf{F}_N$ is general and may be obtained through a number of suitable fluid models, including CFD. For the purposes of this work, we consider DBET and UVLM fluid models because the computational resources required to resolve $\mathbf{F}_N$ are minimal compared to CFD.

Deformable Blade Element Fluid Model

To formulate the DBET fluid model (Fig. 2), we assume a generic aerodynamic force per unit area $dF_{aero,[\cdot]}$ can be represented as

$$dF_{aero,[\cdot]} = \frac{1}{2} C_{[\cdot]} \rho_f \dot{\mathbf{R}} \cdot \dot{\mathbf{R}} \, dS \tag{17}$$

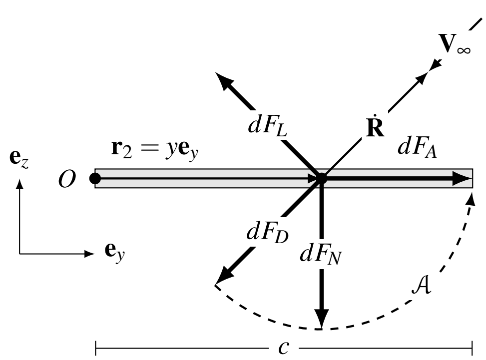

FIGURE 2. Free body diagram of differential aerodynamic forces acting at the location of dm for DBET fluid model. Wing shown in undeformed configuration.

where ρ_f is fluid density, $C_{[\cdot]}$ is an empirical aerodynamic coefficient, $[\cdot]$ is a placeholder to indicate lift of drag, and dS is the differential surface over which the force acts. For the 2D case, $dS = h\,dy$, where h is the wing span (out the page, along the x direction) and dy is a differential length in the chord-wise y direction. The aerodynamic angle-of-attack $\mathcal{A}$ is defined as the angle between the induced flow velocity $\mathbf{V}_\infty$ (equal in magnitude and opposite in direction to $\dot{\mathbf{R}}$ assuming no free-stream flow) and the positive y axis, and can be written as

$$\mathcal{A} = \tan^{-1}\left(\frac{-\dot{\mathbf{R}} \cdot \mathbf{e}_z}{-\dot{\mathbf{R}} \cdot \mathbf{e}_y}\right) = \tan^{-1}\left(\frac{\dot{Z}\cos\theta + y\dot{\theta} + \dot{W}}{\dot{Z}\sin\theta - W\dot{\theta}}\right) \tag{18}$$

As indicated by the above, $\mathcal{A}$ varies along the chord and depends on both the wing's rigid body motion and elastic deformation. The form of aerodynamic lift/drag coefficients in Eq. 17 is taken from [23] as

$$C_L(\mathcal{A}) = C_{L_{max}} \sin(2\mathcal{A}) \tag{19}$$

$$C_D(\mathcal{A}) = \frac{C_{D_{max}} + C_{D_0}}{2} - \frac{C_{D_{max}} - C_{D_0}}{2} \cos(2\mathcal{A}) \tag{20}$$

where $C_{L_{max}}$, $C_{D_{max}}$ and C_{D_0} are empirically fit from experimental or computational methods. Then, expanding Eq. 17 and integrating over the wing surface gives

$$F_{R,[\cdot]} = \frac{1}{2}\rho_f C_{[\cdot]} \int_S (\dot{Z}^2 + 2\dot{Z}\dot{\theta}y\cos\theta + y^2\dot{\theta}^2) \, dS \tag{21}$$

$$F_{E,[\cdot]} = \rho_f C_{[\cdot]} \int_S (-\dot{Z}\dot{\theta}\sin\theta W + [\dot{Z}\cos\theta + \dot{\theta}y]\dot{W}) \, dS \tag{22}$$

where F_R and F_E are the rigid and elastic components of $F_{aero,[\cdot]}$ respectively. Note the terms of $\mathcal{O}(W^2)$ are neglected from F_E given that W is infinitesimal. We then rotate lift and drag forces by $\mathcal{A}$ to determine the aerodynamic axial force $\mathbf{F}_A$ and normal force $\mathbf{F}_N$ as

$$\mathbf{F}_A = (F_D \cos\mathcal{A} - F_L \cos\mathcal{A})\langle \mathbf{e}_y \rangle \tag{23}$$

$$\mathbf{F}_N = (F_D \sin\mathcal{A} + F_L \cos\mathcal{A})\langle -\mathbf{e}_z \rangle \tag{24}$$

In addition to lift and drag forces, we must also consider the normal force imparted to the wing by added mass. The air mass accelerated as the wing flaps may be considerable compared to the mass of the wing itself. This imparts an additional force normal to the wing that is proportional to the wing's acceleration. Added mass normal to the wing, denoted $\mathbf{F}_{N,AM}$ and modified from [24], can be represented for the flapping wing as

$$\mathbf{F}_{N,AM} = -\pi\rho_f \left(\frac{c}{4}\right) \int_S \ddot{\mathbf{R}} \cdot \mathbf{e}_z \, dS \, \langle \mathbf{e}_z \rangle \tag{25}$$

As with lift and drag, it is possible to represent $\mathbf{F}_{N,AM}$ as rigid and elastic components:

$$\mathbf{F}_{N,AM,rigid} = -\pi\rho_f \left(\frac{c}{4}\right) \int_S (\ddot{Z}\cos\theta + y\ddot{\theta})\, dS \langle \mathbf{e}_z \rangle \tag{26}$$

$$\mathbf{F}_{N,AM,elastic} = -\pi\rho_f \left(\frac{c}{4}\right) \int_S (-W\dot{\theta}^2 + \ddot{W})\, dS \langle \mathbf{e}_z \rangle \tag{27}$$

Finally, we combine the aerodynamic normal force $\mathbf{F}_N$ with the fluid force due to added mass $\mathbf{F}_{N,AM}$ and substitute them into Eq. 16 to estimate the non-conservative forces acting on the wing.

Unsteady Vortex Lattice Fluid Model

To employ UVLM (Fig. 3), we assume the flow to be incompressible throughout, and irrotational except on the surface of the wing and in the wake shed from the trailing edge. Using this approach, unsteady effects such as added mass may be accounted for. The wing is discretized into N_p panels of differential length $ds = c/N_p$, with the leading edge of the first panel at O. On each panel, a bound vortex is placed $0.25ds$ aft of the leading edge, and the control point (Cp) is located at $0.75ds$ aft the leading edge [25].

The no-penetration condition states that across the wing surface, the flow velocity component that is normal to the surface must be zero [26], which implies

$$(-\dot{\mathbf{R}} + \mathbf{V}_{BV} + \mathbf{V}_W) \cdot \mathbf{n} = 0 \tag{28}$$

where $\mathbf{V}_{BV}$ is the velocity induced by the bound vortices on the wing, $\mathbf{V}_W$ is the velocity induced by the free wake vortices and $\mathbf{n}$ is the surface normal vector. In this lumped vortex method, this boundary condition is satisfied at the control point of each panel. Enforcing this boundary condition at each control point gives the strength of the bound vortices. Then, the Kelvin-Helmholtz theorem states that the circulation Γ around a closed curve must remain constant, which leads to

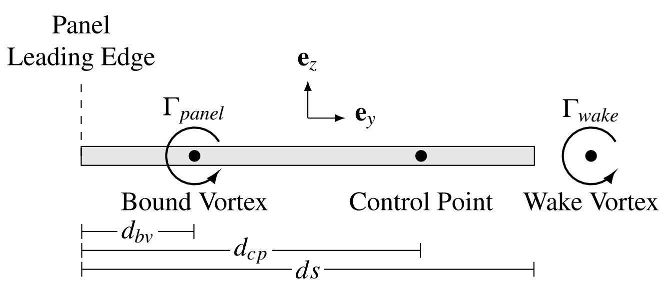

FIGURE 3. Schematic of panel for UVLM fluid model. d_{bv} and d_{cp} are the distance of the bound vortex and control point from the panel leading edge, respectively. ds is panel width.

$$\frac{D\Gamma}{Dt} = 0 \tag{29}$$

Since the initial vorticity is zero, the total bound vorticity and wake vorticity will sum to zero every time step. This condition sets the strength of the newly created wake vortex, and means that the strength of the free vortices remain unchanged [21].

The velocity at point i induced by a vortex at point j, $\mathbf{V}_{ind_{i,j}}$, is given by the Biot-Savart law:

$$\mathbf{V}_{ind_{i,j}} = \frac{\Gamma_j}{2\pi L^2} \langle (Z_j - Z_i)\mathbf{e}_Y + (Y_i - Y_j)\mathbf{e}_Z \rangle \tag{30}$$

where L is the scalar distance between i and j, and Y, Z are the coordinate locations of i and j in the $Y-Z$ plane. The bound vortex strength Γ_i of each panel and the new wake vortex $\Gamma_{(Np+1)}$ are found by simultaneously enforcing the boundary condition at each control point [27], or

$$\begin{bmatrix} a_{1,1} & a_{1,2} & \dots & a_{1,Np} & a_{1,Np+1} \\ a_{2,1} & a_{2,2} & \dots & a_{2,Np} & a_{2,Np+1} \\ \vdots & \vdots & \ddots & \vdots & \vdots \\ a_{Np,1} & a_{Np,2} & \dots & a_{Np,Np} & a_{Np,Np+1} \\ 1 & 1 & 1 & 1 & 1 \end{bmatrix} \begin{bmatrix} \Gamma_1 \\ \Gamma_2 \\ \vdots \\ \Gamma_{Np} \\ \Gamma_{Np+1} \end{bmatrix} = \begin{bmatrix} \text{rhs}_1 \\ \text{rhs}_2 \\ \vdots \\ \text{rhs}_{Np} \\ \text{rhs}^* \end{bmatrix} \tag{31}$$

where $a_{i,j}$ is the component of velocity at the i^{th} control point induced by the unit-strength j^{th} bound vortex that is normal to panel i. This influence coefficient is found using the Biot-Savart law above substituting 1 for Γ_j. The right-had side, rhs_i is the normal component of velocity at the control point due to flapping kinematics and the wake vortices. rhs^* is the sum of the bound vortices on the wing from the previous time step. Γ_{Np+1} is the strength of the newly shed vortex wake, equal to the negative of the change in total bound vorticity from the previous time step.

If we assume the wake convects with the local flow, the velocity of the i^{th} wake $\mathbf{V}_{W,i}$ is the sum of the velocities induced by the wing-bound vortices and the wake vortices, written as

$$\mathbf{V}_{W,i} = \sum_{j=1}^{N_p} \mathbf{V}_{ind_{i,j}} + \sum_{m=1}^{N_p} \mathbf{V}_{ind_{im}}; \quad m \neq i \tag{32}$$

The newly formed wake is placed 0.05c with respect to the wing's trailing edge. Next, to determine the pressure differential across the i^{th} panel, ΔP_i, we employ the unsteady Bernoulli equation

$$\Delta P_i = -\rho_f \left[(-\dot{\mathbf{R}} + \mathbf{V}_W)_i \cdot \tau_i \frac{\Gamma_i}{ds} + \frac{\partial}{\partial t} \sum_{j=1}^{i} \Gamma_j \right] \tag{33}$$

where τ_i is the unit vector tangent to the i^{th} panel, and a positive ΔP indicates lower pressure on the upper surface of the wing. Finally, the fluid normal force acting on the i^{th} panel, $\mathbf{F}_{N_i}$ is

$$\mathbf{F}_{N_i} = \Delta P_i \, c \, ds (\mathbf{n}_i \cdot \mathbf{e}_z) \mathbf{e}_z \tag{34}$$

Equation 34 is then substituted into Eq. 16 to determine the generalized aerodynamic modal force.

SIMULATION

In this section, we compare the results of the two flapping wing FSI models. We first establish the wing's properties and prescribed kinematics based off known values for the Hawkmoth *Manduca sexta*, a common model organism in the study of insect flight. We then analyze the wing tip deflection and aerodynamic forces predicted by both models.

Simulation Parameters

The physical properties of the wing are given in Tab. 1. The chord width, span, thickness were estimated for the Hawkmoth from [28]. We adjust the Young's modulus within the biological values presented in [28] until we achieve a natural frequency of 80 Hz, which is corresponds to the torsional mode of the Hawkmoth wing [29]. The damping ratio is also taken from this source. We treat the wing as a homogenous beam with fixed-free boundary conditions, and thus determine its natural frequency and mass-normalized mode shape analytically using well-known expressions from [30]. However, we stress that this formulation permits material and geometry properties to vary along the wing's y direction. For sake of simplicity, we retain only one vibration mode.

Next, we prescribe the rigid body kinematics of the flapping wing. We note that flapping wings undergo three-dimensional rotation in practice, and that the kinematics presented here are an idealization. We assume that the both pitching and plunging motions are harmonic and out-of-phase by $\frac{\pi}{2}$ radians. The plunging motion represents the large, sweeping flapping rotation of the wing – we are essentially projecting the wing's stroke plane onto a two-dimensional space when employing the pitch-plunge model. The pitching has a similar interpretation in both 2D and

TABLE 1. Physical properties of the wing used for simulation.

Symbol	Description	Value	Units
E	Young's Modulus	24.5	GPa
c	Chord Width	2	cm
h	Span	5	cm
t	Thickness	40	μm
M_w	Mass	40	μg
ω_1	First Natural Frequency	80	Hz
ζ_1	First Modal Damping Ratio	0.05	-

3D models. All flapping kinematics are summarized in Tab. 2. Rotation/translation amplitudes are similar to those presented in [13], whereas the flapping frequency is taken from [31]. We use a lower pitch amplitude than is typically observed in Hawkmoth flight [31]. This is because pitch measurements from flying insects, particularly those that experience large wing twisting, invariably contain some rotation arising from rigid body rotation and elastic deformation. How the rigid body rotation and elastic deformation sum to net wing pitch is challenging to delineate from experimental measurements in free-flying insects.

TABLE 2. Flapping Kinematics Parameters.

Symbol	Description	Value	Units
Z_0	Plunge Amplitude	2	cm
θ_0	Pitch Amplitude	15	$^\circ$
ϕ_z	Plunge Phase Advance	90	$^\circ$
ω	Flapping Frequency	25	Hz

We now establish the simulation parameters used for both fluid models. In both cases, we use a time step that corresponds to 200 intervals per wingbeat period (0.2 ms) and allow the simulation to run for 15 periods, which we determined was an adequate duration to achieve steady-state in all cases considered. Reducing the time step further did not impact the solution.

We then verify that the numerical methods have converged. First, consider the DBET model. The solution accuracy, as well as the time required to solve, are dependent on the number of blade elements the structure is discretized into. To ensure that the solution has converged, we vary the number of blade elements and record the maximum wing tip deflection. Then, we plot the wingtip displacement normalized by the converged wingtip displacement with respect to the number of elements (Fig. 4). The solution converges quickly, with less than a 1%

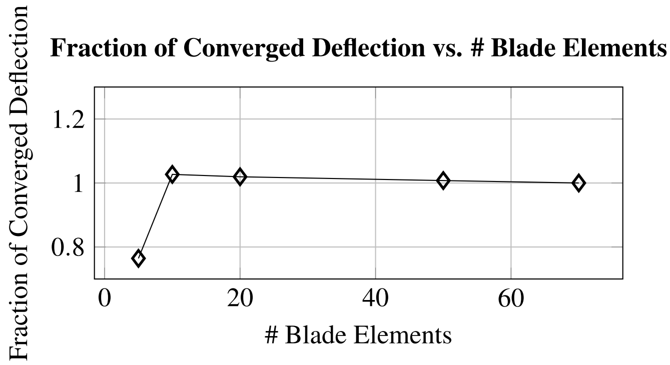

FIGURE 4. Convergence study for the DBET fluid model showing the dependence of the solution on number of blade elements. The y-axis shows the maximum wingtip deflection for the current parameters as a fraction of the maximum wingtip deflection at convergence.

change when increasing the total element count beyond 5. While this rapid convergence can greatly expedite the time required to solve the DBET model, it is worth noting that wings with non-homogeneous material or geometric properties will require more elements to resolve.

Next, consider the UVLM model. We determined that the solution was most sensitive to the number of panels and wakes considered. We maintain the number of wakes at 200 and vary the panel count from 5 to 70, and then maintain the number of panels at 50 and vary the wake count from 5 to 300. We again plot the normalized wingtip displacement as a function of these parameters (Fig. 5). In both cases, the solution converges relatively quickly, with the solution being modestly more sensitive to the number of wakes considered.

With these simple convergence studies completed, we define the remaining parameters needed to carry out numerical simulations for both models. DBET parameters are shown in Tab. 3, where the aerodynamic coefficients are similar to those in [23]. UVLM parameters are shown in Tab. 3.

TABLE 3. DBET Simulation Parameters.

Symbol	Description	Value
C_{D_0}	Drag offset coefficient	0.4
$C_{D_{max}}$	Maximum drag coefficient	4.0
$C_{L_{max}}$	Maximum lift coefficient	1.8
N	Number of blade elements	50

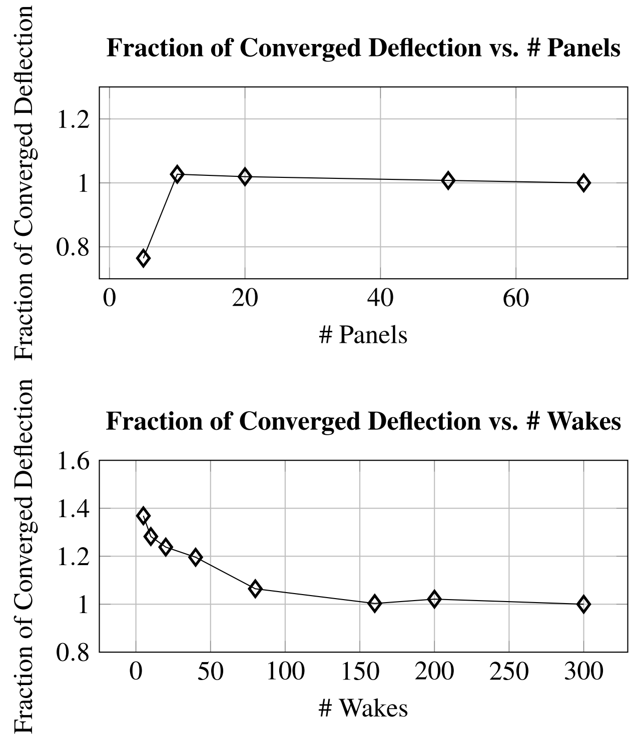

FIGURE 5. Convergence study for the UVLM fluid model showing the dependence of the solution on (top) number of panels and (bottom) number of wakes. The y-axis shows the maximum wingtip deflection for the current parameters as a fraction of the maximum wingtip deflection at convergence.

TABLE 4. UVLM Simulation Parameters.

Symbol	Description	Value
N_w	Number of wakes	200
N_p	Number of panels	50
d_{cp}	Control point distance from leading edge as % of panel length	75
d_{bv}	Bound vortex distance from leading edge as % of panel length	25

Model Comparison

We first compare BET and UVLM fluid models for a rigid wing to provide a baseline and to assess how well the two agree before flexibility is incorporated. The aerodynamic normal force $\mathbf{F}_N$ predicted by both fluid models is shown as a function of a single wingbeat in Fig. 6. In general, the two models agree well both in terms of magnitude and phase. UVLM predicts a larger normal force magnitude and leads the BET prediction in phase. These discrepancies are relatively minor, which suggests the simulation parameters provide a good basis for the fluid models, at least when the wing is rigid.

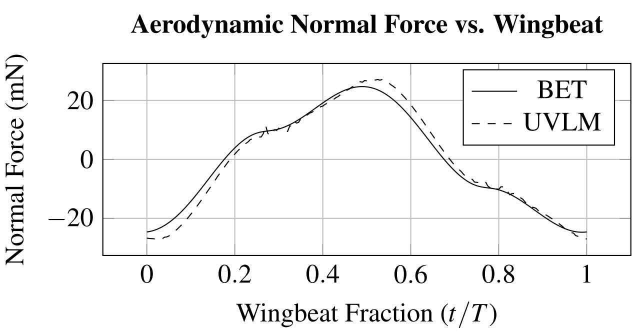

FIGURE 6. Aerodynamic normal force $\mathbf{F}_N$ for a rigid wing predicted by BET and UVLM solvers.

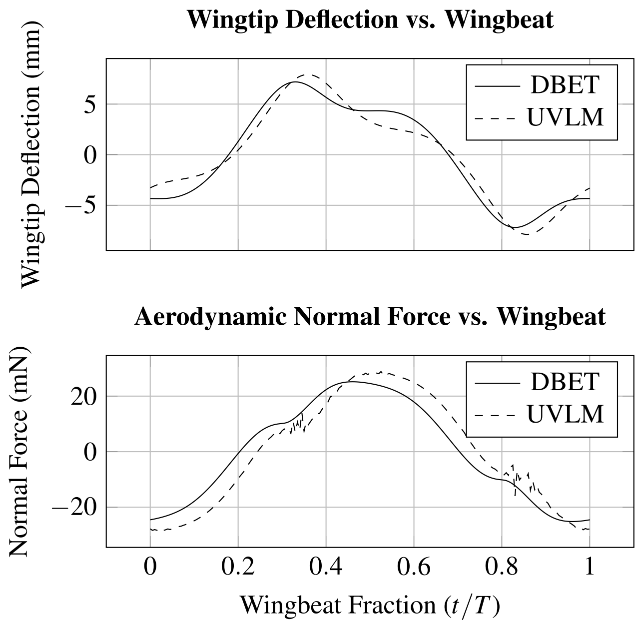

FIGURE 7. (Top) Wingtip deflection and (Bottom) aerodynamic normal force $\mathbf{F}_N$ for a flexible wing predicted by BET and UVLM solvers.

Then, we permit the wing to deform under inertial and aerodynamic loads. Recall that both FSI models utilize the same structural framework, and therefore any differences in the wing's response between the two models stem from differences in the fluid models. We plot both the wingtip (at $y = c$) deflection as well as aerodynamic normal forces for the flexible wing over a wingbeat period in Fig. 7. DBET and UVLM models predict wingtip deflections similarly, with maximum deflections of approximately 7.5 mm occurring just after the stroke reversal around t/T = 0.33, 0.83. DBET predicts a larger 3ω component of wingtip response as well as a phase lag relative to UVLM. This phase discrepancy is more appreciable in the aerodynamic normal force, where the DBET normal force lags the UVLM normal force by approximately 18°. While the phase discrepancy appears small, we point out that even minor phase changes can significantly affect aerodynamic force production in the inertial frame, which is essential to flight. Moving forward, we will make efforts to reconcile any phase differences between the two models, particularly once a high-fidelity CFD simulation is available.

From a computational point of view, the DBET model took 2.95 seconds to solve while the UVLM model took 46.81 seconds to solve, each over 15 wingbeats. It is worth noting that the solution time per wingbeat is relatively stable throughout the DBET simulation, whereas the solution time per wingbeat increases at the beginning of the UVLM simulation and later stabilizes once the maximum number of retained wakes is reached. Nonetheless, on an average time-per-period basis, the DBET model solves roughly 15 times faster than UVLM, representing a large computational savings. Compared to coupled CFD-FEA, both UVLM and DBET are several orders of magnitude faster.

Lastly, we study the influence that flexibility has on mean vertical aerodynamic force production (aligned with the -Y direction; Fig. 1), a relevant quantity to keeping the insect aloft. We consider the flapping kinematics in Tab. 2, and solve for the mean aerodynamic vertical force using both DBET and UVLM for both rigid and flexible wings. The results are summarized in Tab. 5. In both cases, the flexible wing produces more mean vertical force, with increases of 7% and 116% from the rigid wing as predicted by the DBET and UVLM models, respectively. We believe in this case, the UVLM model is severely overpredicting the aerodynamic benefits of wing deformation. The DBET model indicates that viscous drag increases significantly as the wing deforms. The UVLM model considers only pressure drag and cannot account for viscous drag without an empirical or other corrective model. This issue affects vector aerodynamic force production, even when the normal forces component predicted by UVLM and DBET are similar (Fig. 7).

TABLE 5. Influence of wing flexibility on mean vertical force for both fluid solvers.

Fluid Solver	Wing Type	Mean Vertical Force (mN)
DBET	Rigid	2.76
DBET	Flexible	2.97
UVLM	Rigid	3.08
UVLM	Flexible	6.67

CONCLUSION

In this work, we derived a reduced-order flapping wing FSI model, where the wing was idealized as a two-dimensional flexible pitching, plunging airfoil. We considered DBET and UVLM fluid models, where the former is more computational efficient but does not provide information regarding the flow surrounding the wing, and the latter partially resolves the flow structure but requires increased solution time. We found that, for a limited set of kinematics, DBET and UVLM produced similar estimates for wingtip deflection as well as aerodynamic normal forces. DBET solved approximately 15 times faster than UVLM though both fluid models are much quicker relative to direct numerical simulation. However, UVLM appears to overestimate the vector sum of aerodynamic forces produced by the wing, perhaps because it cannot account for viscous drag without modification. We believe the 7% increase in mean aerodynamic vertical force predicted by the DBET model is a more accurate reflection of the benefits of wing flexibility on force production. While this aerodynamic benefit may seem small, it is plausible that flexibility is also reducing the energy required to flap. Thus, both energy and force production should be studied simultaneously moving forward.

The primary contribution of this work is the DBET framework, which extends the most common aerodynamic model used to study flapping wing insect flight to incorporate flexibility. Nonetheless, there remain many factors to consider before the DBET model is generally applicable, even for the 2D case. Most importantly, we must explore a large range of kinematic parameters and wing stiffnesses. While DBET and UVLM agree fairly well for most responses considered here, it is possible this agreement deteriorates for kinematics that include larger rotations and/or plunging angle. Further, UVLM itself must be verified for accuracy against higher-order CFD, particularly because it does not model viscous forces in this current form. Despite these limitations, the research presented here provides a solid foundation for further studies in reduced-order modeling of flapping wing FSI.

ACKNOWLEDGMENT

This research was supported the National Science Foundation under awards Nos. CBET-1855383 and CMMI-1942810. Any opinions, findings, and conclusions or recommendations expressed in this material are those of the author(s) and do not necessarily reflect the views of the National Science Foundation.

REFERENCES

[1] Phan, H. V., and Park, H. C., 2019. "Insect-inspired, tailless, hover-capable flapping-wing robots: Recent progress, challenges, and future directions". *Progress in Aerospace Sciences*, p. 100573.

[2] Farrell Helbling, E., and Wood, R. J., 2018. "A review of propulsion, power, and control architectures for insect-scale flapping-wing vehicles". *Applied Mechanics Reviews,* ***70***(1).

[3] Combes, S. A., and Daniel, T. L., 2003. "Into thin air: contributions of aerodynamic and inertial-elastic forces to wing bending in the hawkmoth manduca sexta". *Journal of Experimental Biology,* ***206***(17), pp. 2999–3006.

[4] Mountcastle, A. M., and Combes, S. A., 2013. "Wing flexibility enhances load-lifting capacity in bumblebees". *Proceedings of the Royal Society B: Biological Sciences,* ***280***(1759), p. 20130531.

[5] Jankauski, M., Guo, Z., and Shen, I., 2018. "The effect of structural deformation on flapping wing energetics". *Journal of Sound and Vibration,* ***429***, pp. 176–192.

[6] Dickerson, B. H., Aldworth, Z. N., and Daniel, T. L., 2014. "Control of moth flight posture is mediated by wing mechanosensory feedback". *Journal of Experimental Biology,* ***217***(13), pp. 2301–2308.

[7] Shyy, W., Aono, H., Chimakurthi, S. K., Trizila, P., Kang, C.-K., Cesnik, C. E., and Liu, H., 2010. "Recent progress in flapping wing aerodynamics and aeroelasticity". *Progress in Aerospace Sciences,* ***46***(7), pp. 284–327.

[8] Tian, F.-B., Dai, H., Luo, H., Doyle, J. F., and Rousseau, B., 2014. "Fluid–structure interaction involving large deformations: 3d simulations and applications to biological systems". *Journal of computational physics,* ***258***, pp. 451–469.

[9] Takizawa, K., Tezduyar, T. E., and Kostov, N., 2014. "Sequentially-coupled space–time fsi analysis of bio-inspired flapping-wing aerodynamics of an mav". *Computational Mechanics,* ***54***(2), pp. 213–233.

[10] Jankauski, M., and Shen, I., 2014. "Dynamic modeling of an insect wing subject to three-dimensional rotation". *International Journal of Micro Air Vehicles,* ***6***(4), pp. 231–251.

[11] Jankauski, M., and Shen, I., 2016. "Experimental studies of an inertial-elastic rotating wing in air and vacuum". *International Journal of Micro Air Vehicles,* ***8***(2), pp. 53–63.

[12] Anderson, J. D., and Wendt, J., 1995. *Computational fluid dynamics*, Vol. 206. Springer.

[13] Yin, B., and Luo, H., 2010. "Effect of wing inertia on hovering performance of flexible flapping wings". *Physics of Fluids,* ***22***(11), p. 111902.

[14] Tian, F.-B., Luo, H., Song, J., and Lu, X.-Y., 2013. "Force production and asymmetric deformation of a flexible flapping wing in forward flight". *Journal of Fluids and Structures,* ***36***, pp. 149–161.

[15] Sridhar, M., and Kang, C.-k., 2015. "Aerodynamic performance of two-dimensional, chordwise flexible flapping wings at fruit fly scale in hover flight". *Bioinspiration & biomimetics,* ***10***(3), p. 036007.

[16] Roccia, B. A., Preidikman, S., and Balachandran, B., 2017.

"Computational dynamics of flapping wings in hover flight: a co-simulation strategy". *AIAA Journal,* ***55***(6), pp. 1806–1822.

[17] Wang, Q., Goosen, J., and van Keulen, F., 2017. "An efficient fluid–structure interaction model for optimizing twistable flapping wings". *Journal of Fluids and Structures,* ***73***, pp. 82–99.

[18] Schwab, R. K., Reid, H. E., and Jankauski, M., 2020. "Reduced-order modeling and experimental studies of bilaterally coupled fluid-structure interaction in single-degree-of-freedom flapping wings (in press)". *Journal of Vibration and Acoustics*.

[19] Schwab, R. K., Reid, H. E., and Jankauski, M. A., 2019. "Reduced-order modeling and experimental studies of two-way coupled fluid-structure interaction in flapping wings". In ASME 2019 International Design Engineering Technical Conferences and Computers and Information in Engineering Conference, American Society of Mechanical Engineers Digital Collection.

[20] Schwab, R., Johnson, E., and Jankauski, M., 2019. "A novel fluid–structure interaction framework for flapping, flexible wings". *Journal of Vibration and Acoustics,* ***141***(6).

[21] Fitzgerald, T., Valdez, M., Vanella, M., Balaras, E., and Balachandran, B., 2011. "Flexible flapping systems: computational investigations into fluid-structure interactions". *The Aeronautical Journal,* ***115***(1172), pp. 593–604.

[22] Mountcastle, A., and Daniel, T., 2010. "Vortexlet models of flapping flexible wings show tuning for force production and control". *Bioinspiration & biomimetics,* ***5***(4), p. 045005.

[23] Whitney, J. P., and Wood, R. J., 2010. "Aeromechanics of passive rotation in flapping flight". *Journal of Fluid Mechanics,* ***660***, pp. 197–220.

[24] Sedov, L. I., Chu, C., Cohen, H., Seckler, B., and Gillis, J., 1965. "Two-dimensional problems in hydrodynamics and aerodynamics". *Physics Today,* ***18***, p. 62.

[25] Katz, J., and Plotkin, A., 2001. *Low-speed aerodynamics*, Vol. 13. Cambridge university press.

[26] Roccia, B. A., Preidikman, S., Massa, J. C., and Mook, D. T., 2013. "Modified unsteady vortex-lattice method to study flapping wings in hover flight". *AIAA journal,* ***51***(11), pp. 2628–2642.

[27] Tang, L., Paı, M. P., et al., 2007. "On the instability and the post-critical behaviour of two-dimensional cantilevered flexible plates in axial flow". *Journal of Sound and Vibration,* ***305***(1-2), pp. 97–115.

[28] Combes, S., and Daniel, T., 2003. "Flexural stiffness in insect wings i. scaling and the influence of wing venation". *Journal of experimental biology,* ***206***(17), pp. 2979–2987.

[29] Sims, T. W., Palazotto, A. N., and Norris, A., 2010. "A structural dynamic analysis of a manduca sexta forewing". *International Journal of Micro Air Vehicles,* ***2***(3), pp. 119–140.

[30] Meirovitch, L., 2010. *Fundamentals of vibrations*. Waveland Press.

[31] Willmott, A. P., and Ellington, C. P., 1997. "The mechanics of flight in the hawkmoth manduca sexta. i. kinematics of hovering and forward flight.". *Journal of experimental Biology,* ***200***(21), pp. 2705–2722.

APPENDIX A - KINETIC ENERGY

This appendix provides additional detail on the derivation of Eq. 11. In general, the Lagrange formulation requires explicit representations of kinetic energy T and potential energy U. Expanding Eqs. 9-10 in terms of Eqs. 6,8 yields

$$\begin{aligned}
T_1 &= \frac{1}{2}\dot{\theta}^2\int_m W^2\,dm = \frac{1}{2}\dot{\theta}^2\sum_{k=1}^{\infty} q_k^2 \\
T_2 &= -\dot{\theta}\dot{Z}\sin\theta\int_m W\,dm = -\dot{\theta}\dot{Z}\sin\theta\sum_{k=1}^{\infty} q_k\int_m \phi_k\,dm \\
T_3 &= \frac{1}{2}\dot{Z}^2\int_m dm = \frac{1}{2}m\dot{Z}^2 \\
T_4 &= \frac{1}{2}\dot{\theta}^2\int_m y^2 dm = \frac{1}{2}I_{xx}\dot{\theta}^2 \\
T_5 &= \frac{1}{2}\int_m \dot{W}^2\,dm = \frac{1}{2}\sum_{k=1}^{\infty}\dot{q}_k^2 \\
T_6 &= \dot{Z}\cos\theta\int_m y\,dm \\
T_7 &= \dot{\theta}\int_m \dot{W}y\,dm = \dot{\theta}\sum_{k=1}^{\infty}\dot{q}_k\int_m \phi_k y\,dm \\
T_8 &= \dot{Z}\cos\theta\int_m \dot{W}\,dm = \dot{Z}\cos\theta\sum_{k=1}^{\infty}\dot{q}_k\int_m \phi_k\,dm \\
U &= \frac{1}{2}\int_V S(W,W)\,dV = \frac{1}{2}\sum_{k=1}^{\infty}\omega_k^2 q_k^2
\end{aligned}$$

where $T = \sum_{m=1}^{8} T_m$. Then, to determine the equation of motion governing q_k, we apply the Lagrangian formulation. Treating q_k as our generalized coordinate, we have

$$\frac{d}{dt}\left(\frac{\partial T}{\partial \dot{q}_k}\right) - \frac{\partial T}{\partial q_k} + \frac{\partial V}{\partial q_k} = Q_k$$

Carrying out the above operations results in Eq. 11.